Journal of
Microelectromechanical Systems

A Large Range of Motion 3D MEMS Scanner with Five Degrees of Freedom

Lawrence K. Barrett, Thomas Stark, Jeremy Reeves, Richard Lally, Alexander Stange, Corey Pollock, Matthias Imboden, and David J. Bishop, *Member, IEEE*

***Abstract*— Here, we discuss a novel, mixed mode 3D XYZ scanner built within a single foundry process. The device has a large range of motion in X, Y and Z (14.1 μm in X,Y and 97.9 μm in Z) and can also rotate about two axes (7.4°), making it a 5 degree of freedom scanner. Vertical actuation can be accomplished with both thermal actuators, which have a larger range of motion, and capacitive actuators, which are faster, responding fully up to 3.2 kHz. Although useful for many applications, including scanning probe microscopy, micrometer scale optical microscopy, and manipulation of biological objects, the device was designed to be a 3D scanner for spray-painting atoms upon a surface with nanoscale precision and resolution for nanofabrication. Demonstrating the ability to combine the device with other complicated MEMS systems, it is integrated with an XY scanner designed to serve as a shutter of atomic flux. The full system has 7 degrees of freedom and 12 actuation motors, and because it is built in a low cost commercial foundry with a robust, stable process, it is easy and inexpensive to fabricate multiple copies or integrate into other complicated systems, making a system of systems.**

***Index Terms*— Comb Drive, Electrostatic Actuators, Nanopositioning, MEMS, Position Control, Thermal Actuators.**

I. Introduction

THE ability to position and manipulate objects on the nanoscale is extremely valuable in modern technology. Applications of nanopositioning systems include micrometer scale optical microscopy [1]–[5], scanning probe microscopy (SPM) [6]–[8], optical beam steering [9], [10], nanomanufacturing [11], [12], and the manipulation of cells and other biological materials [13], [14]. This list is certainly not exhaustive and it is likely that many more applications will be created as nanotechnology continues to develop.

MEMS have several potential advantages in nanopositioning. Due to their scale, they can have high resolutions, high resonant frequencies, high quality factors, and small footprints. In addition, their fabrication processes are low cost per device and allow for high device to device uniformity [15], [16]. Consequently, a variety of MEMS nanopositioners with three translational degrees of freedom (DoF) have been developed [1], [7], [17]–[21]. Most of these devices rely on electrostatic actuation methods which are fast, low power, and are highly repeatable [15], [16]. Some of these devices require extra assembly or off chip components [1], [18], [19]. Others have limited (<5 μm) vertical range of motion [7], [17].

One of the most complete electrostatic actuators has been demonstrated by Correa *et al*. [22] and Koo *et al*. [20] in their partner articles. Their device is capable of moving in a 20 μm cube using a silicon-on-insulator (SOI) process and closed loop control. Another device, demonstrated by Chen *et al*., is capable of moving in the three translational degrees of freedom with ranges of 8.4 μm × 12.8 μm × 8.8 μm and the three angular degrees of freedom with ranges of 1.1° × 1.0° × 1.9°. The device relies on thermal actuation methods and was made using deep reactive ion etching (DRIE) [21].

As part of an ongoing effort to develop a nanomanufacturing technique based on MEMS systems [11], [12], [23], we developed a system of nanopositioners or scanners consisting of a novel 5 DoF scanner capable of moving in X,Y,Z and rotating about two axis integrated with an XY scanner, as seen in Fig. 1. The technique is called atomic calligraphy, and the idea is to mill nanoscale apertures into the plate of the 5 DoF scanner and use the modified plate as a dynamic stencil to direct the flow of atoms as they are evaporated through a hole in the MEMS substrate onto a target substrate. The 5 DoFs allow the plate to be moved in the desired pattern in X and Y while concurrently the plate can be held parallel to the target using the two axis of rotation and the gap distance between them can be controlled with the Z actuation. The additional XY scanner is useful here as a shutter that can start and stop the flow of atoms rapidly. The atomic calligraphy configuration is outlined in supplemental materials section S1.

In this paper, we focus on the design and behavior of the novel 5 DoF scanner. The XY scanner pictured in Fig. 1 is functional, and its presence demonstrates the ability to easily integrate the 5 DoF scanner with other complicated MEMS systems. It is not discussed in more detail because its design and behavior has been discussed elsewhere [11], [12], [24].

Though designed to be a dynamic stencil, the 5 DoF scanner is generally useful in applications that require positioning on the nanoscale. It utilizes both thermal and electrostatic actuation to position the plate central plate. It is fabricated using the MEMSCAP PolyMUMPs process with no significant post

This work was funded by DARPA Atoms to Product (A2P) Program/Air Force Research Laboratory (AFRL) contract no. FA8650-15-C-7545, the National Science Foundation (NSF Grant No.1361948 and Grant ECCS-1708283), and the Engineering Research Centers Program of the National Science Foundation through NSF Cooperative Agreement under Grant EEC-0812056, Grant EEC-1647837.

L. K. Barrett, T. Stark, R. Lally, and A. Stange are with the Division of Material Science, Boston University, Boston, MA 02215 USA (email: blawrenc@bu.edu; Thomas.joseph.stark@gmail.com; rlally@bu.edu; stange@bu.edu).

J. Reeves is with the Electrical and Computer Engineering Department, Boston University, Boston, MA 02215 USA (email: jbr2@bu.edu).

C. Pollock is with the Department of Mechanical Engineering, Boston University, Boston, MA 02215 USA (email: cpollock@bu.edu)

M. Imboden is with École Polytechnique Fédérale de Lausanne, Institute of Microengineering, Neuchâtel, Switzerland (email: matthias.imboden@epfl.ch)

D. J. Bishop is with the Electrical and Computer Engineering Department, Physics Department, Division of Material Science, Department of Mechanical Engineering, Department of Biomedical Engineering, Boston University, Boston, MA 02215 USA (e-mail: djb1@bu.edu).

Digital Object Identifier: 10.1109/JMEMS.2018.2886653

TABLE I
SUMMARY OF ACTUATION METHODS AND KEY PARAMETER

Actuation Method or Parameter	Design Target Range or Value (Vacuum)	Vacuum Range or Value	Air Range or Value	Sensitivity Vacuum	Sensitivity Air
Lateral Actuation	Maximum Possible	14.1 μm (±7.1 μm)	Same as Vacuum	$3.7*10^{-4}$ μm/V^2	Same as Vacuum
Vertical Actuation Method One-All Combdrives	>20 μm	Same as Air	9.2 μm	Same as Air	0.143 μm/V at 20 V 0.0322 μm/V at 80 V
Vertical Actuation Method Two-Parallel Plate	>20 μm	Same as Air	39.5 μm	Same as Air	0.0139 μm/V^2
Vertical Actuation Method Three-Thermal Bimorphs	>20 μm	97.9 μm	39.5 μm	11.5 μm/V at 4.5 V	0.0322 μm/V at 32 V
Angular Actuation	2° (±1°)	7.4° (±3.7°)	1.8° (±0.89°)	0.423 deg./V	0.0186 deg./V
Initial Height	~120 μm [a]	Same as Air	~118.5 μm [a]	NA	NA

[a]Varies with ambient temperature

processing [25]. Using a low cost commercial foundry with a robust, stable process simplifies the production of devices and streamlines integration with complicated MEMS systems. The scanner is capable of moving 14.1 μm in both translational directions, 97.9 μm vertically, and rotating 7.4° in around both axis. Vertical actuation is achieved using three independent methods. The method providing the largest range of motion relies on thermal actuation and is limited to operating below 10 Hz by the thermal time constant of the system. The other methods use electrostatics with measured responses up to 3.2 kHz.

II. DESIGN

The scanner is designed to meet the needs of atomic calligraphy. While a detailed discussion of atomic calligraphy is beyond the scope of this work, it is worth outlining the targets that influence design decisions. The primary targets for atomic calligraphy are vertical actuation range, plate height, angular actuation range, and lateral actuation range. Vertical actuation accounts for thermal drifts during evaporation and height variations across a target. The target range is >20 μm. The target for the initial height is 120 μm. The height of the plate at all times must clear the height of the electrical bonds ($\sim$80-100 μm in this case). Angular actuation is necessary to position the mask plate parallel to the target plate. 1° in either direction should be sufficient to correct for any misalignments that exist due (largest misalignment seen in current experiments is <0.6°). Actuation in the lateral directions should be as high as possible without sacrificing speed and reliability. Lateral actuation defines the patterns being written. At the end of the actuation range a macro stage must be used to step to a new area. Reducing these steps increases speed and decreases errors in the pattern. These targets are summarized in table one along with the sensitivities and ranges of the various actuation methods and conditions. This section will generally describe the scanner and its operation and discuss design parameters that affect the actuation ranges and initial height.

The scanner, as shown in Fig. 1, is fabricated using the PolyMUMPs process by MEMSCAP. The process includes three polysilicon layers (two of which are moveable) and a gold layer that sit on a silicon nitride coated silicon handle. The device consists of four comb drive actuators each connected to a pair of polysilicon/gold thermal bimorphs. The bimorphs in turn are connected to a central polysilicon plate by a pair of polysilicon tethers which have bends to relieve tension. In the particular device studied here, a second 2 DoF scanner was fabricated under the 5 DoF scanner. This gives the full device 7 DoF that comes from 12 different actuation motors.

Devices come from the foundry with the movable polysilicon layers buried in sacrificial oxide which is removed by etching in hydrofluoric acid (HF) for 15 min. This release time is longer than recommend for a PolyMUMPs device because no holes were put into the central plate to allow for rapid releasing. Release holes could be added to the design, but that is undesirable when using the central plate as a mask. PolyMUMPs devices are known to have a problem with galvanic corrosion during the HF etch, and the issue is exacerbated by the long etching time. We mitigated the problem, using a solution previously demonstrated by Syed *et al*. Breakable tethers were added to electrically connect the device layers to the silicon handle which then serves as a sacrificial anode during the etch [26].

After release, the devices were dried using a critical point dryer (CPD). The CPD prevents device layers from sticking to each other or the substrate. If a device layer does stick, it usually can be separated using a probe station. Once the oxide has been removed, the gold/polysilicon thermal bimorphs bend out of plane due to residual stresses. The bending can

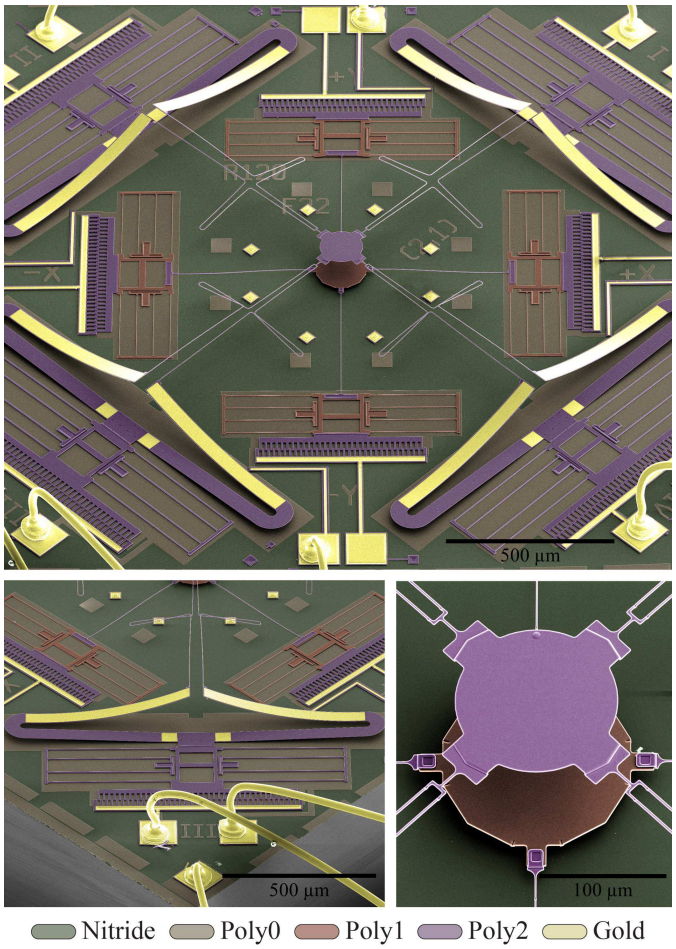

Fig. 1. Colorized SEM images of the full scanner system. The upper image shows the entire device while the two lower images show expanded views of its various parts. The device consists of two movable plates. The upper plate is the 5 DoF scanner and the lower plate is a 2 DoF or XY scanner. The device comprises 8 electrostatic comb drive motors and 4 thermal bimorph motors. Colors represent different device layers in the PolyMUMPs process by MEMSCAP.

be increased by annealing. The devices in this paper were annealed for 5 min. at 210 °C on a hotplate.

The device is designed to position the central plate. It does so using four actuator pairs, each in a separate quadrant, that consist of a comb drive paired with two gold/polysilicon thermal bimorphs, as seen in Fig 1. Generally, the comb drives are used for lateral actuation, and the thermal bimorphs provide vertical and angular motion.

The thermal bimorphs consist of a U-shaped piece of the second polysilicon layer with gold on the entire length of one of the straight sides, as seen in Fig 2b. The other side has a small piece of gold where it attaches to the comb drive. This small gold square is there to prevent that side of the U-shape from sticking or catching by providing it with a small amount of lift, visible in Fig 2c, which also increases the total height of the thermal bimorph to a small degree. Most of the height comes from the all-gold side.

The tops of the bimorphs are attached to the plate via a 2.5 μm wide tether of the second polysilicon layer. Previous

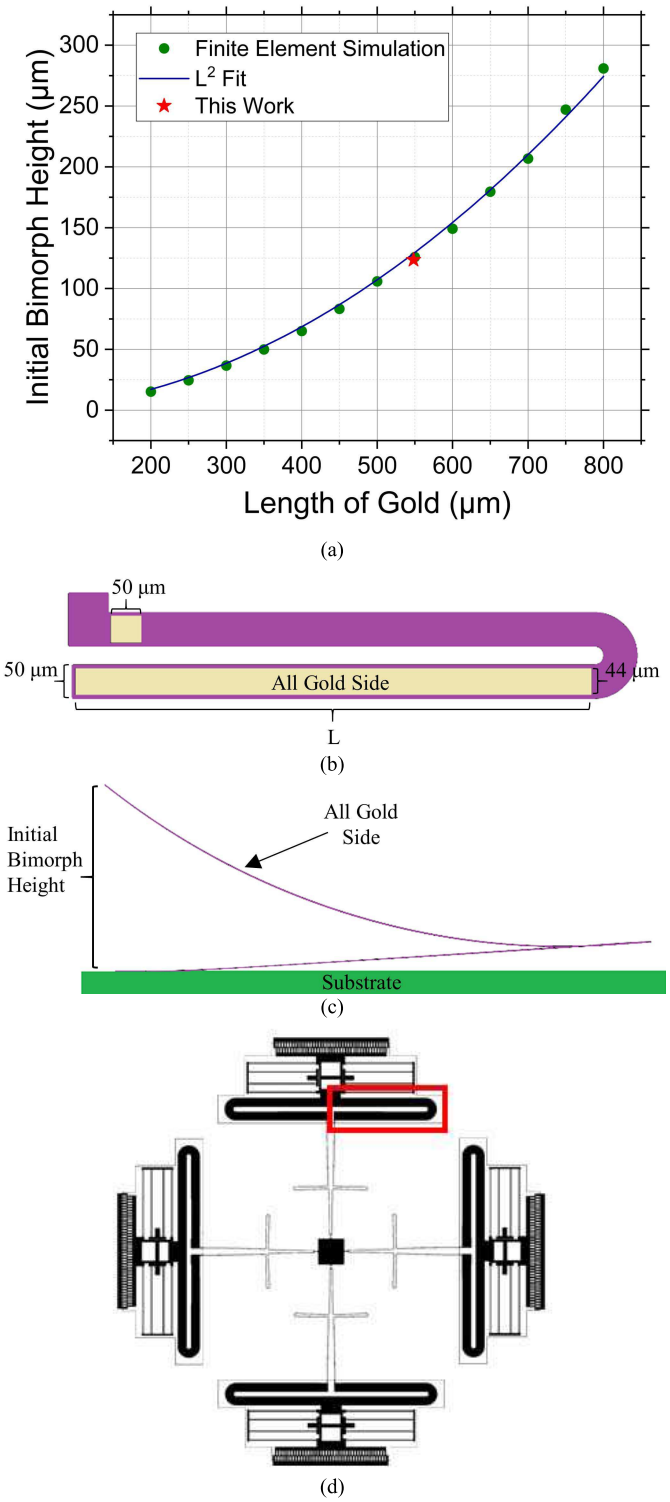

Fig. 2. Finite element analysis simulation of the initial deformation of the U-shaped thermal bimorphs. (a) The relationship between the length of the gold on the all gold side and the initial height of the bimorph. The simulation is well fit by $h = A * L^2$ where A equals $4.29{*}10^{-4}$. (b) Schematic of a U-shaped thermal bimorph. (c) The simulated deformed shape of the U-shaped thermal bimorph due to the stress in the gold. (d) Diagram of the device with a red square showing the location of a U-shaped thermal bimorph (b) and (c) show a U-shaped thermal bimorph with L=800 μm

iterations of this design had straight tethers with no bends in them (Supplemental Materials, S2). At higher actuation

voltages on the comb drive, this design would begin to catch on the substrate because the force of the tether on the top of the bimorph and the spring on the bottom generated enough of a torque to cause the edge of the base to sink and make contact with the substrate. Bends were added to the tethers to relieve some of the strain and decrease the torque on the bimorphs.

The bends also cause the plate to lower a small amount ($\sim$5 μm). This occurs because the bimorphs twist the tethers as they lift and the bend stretches vertically to relieve that twist. Consequently, the bimorph side of the tether is higher than the plate side. It is possible to design the tethers so that the plate side is higher, as can be seen in supplemental materials section S3. This would be desirable if the plate needs to be the highest part of the device. However, these bends are less effective at reducing torque on the bimorphs.

The 5 DoF scanner is actuated using nine independent electrical inputs: the four immovable comb voltages, the four movable comb voltages, and the substrate ground. Angular actuation and the largest range method of vertical actuation function by running current between the movable combs to heat the thermal bimorphs. As the bimorphs heat, the difference in thermal expansion between the gold and the polysilicon cause them to bend downward [15], [27].

The length of the gold on the all gold side of the thermal bimorphs is a key design parameter. It determines the initial bimorph height which is equal to the initial plate height minus a small step down in the strain relief. This plate height largely determines the ranges of both angular actuation and vertical actuation method three in vacuum, as in vacuum the bimorphs will bend down almost to the substrate surface. It also affects the ranges of the other two vertical actuation methods, particularly method two as its range will be one third the initial plate height. The range of the lateral actuation can also be affected because the height of the bimorphs determines the amount of strain relief necessary to prevent catching and the strain relief affects lateral actuation as discussed at the end of this section.

Fig. 2a shows a finite element analysis (FEA) of the connection between the length of the gold on the all gold side and the initial height of the thermal bimorphs. The simulation data is well fit by

$$h = A * L^2 \tag{1}$$

where h is the initial bimorph height in microns, L is the length of the gold in microns, and a is a constant fit parameter. The best fit was found when A was $4.29{*}10^{-4}$. The stress level in the gold in the simulation is set at 260 MPa to match bimorph heights seen experimentally. FEA simulation was done using Comsol Multiphysics.

Lateral positioning is controlled via the potential differences between the movable and immovable combs. The potential generates a force across the capacitive comb which generates a displacement as it is balanced by the mechanical response of the system. The force generated by the comb drive is given below [15].

$$F_{comb} = \left|\frac{\partial U}{\partial x}\right| = \left|\frac{\partial}{\partial x}\left(\frac{1}{2}CV^2\right)\right| \tag{2}$$

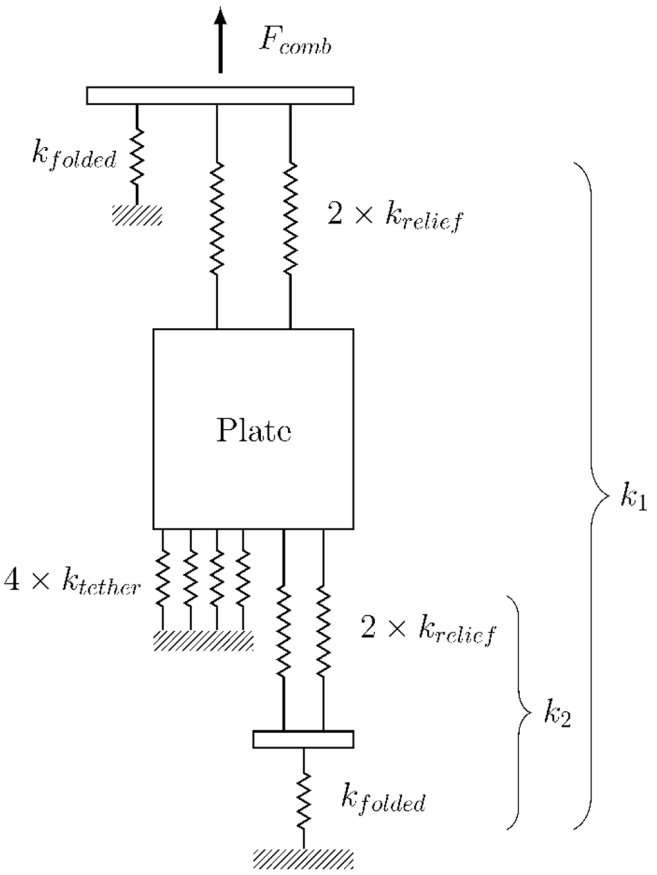

(a)

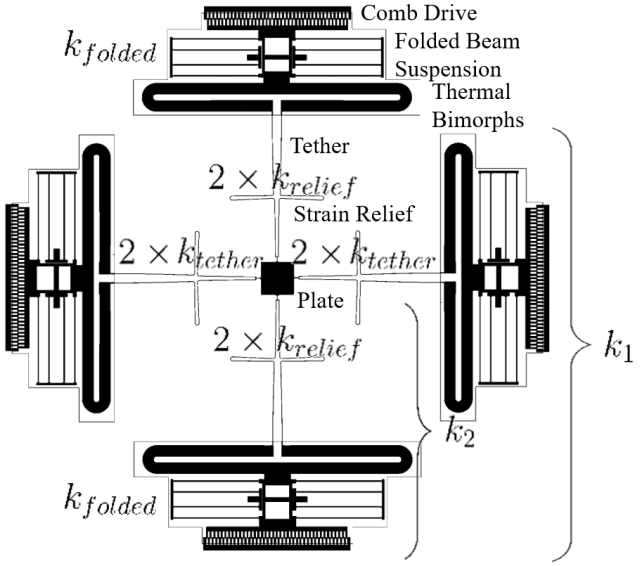

(b)

Fig. 3. Diagrams of the mechanics of the device. (a) Diagram of a spring model of the device, (b) Diagram of the device with different components labeled with their name and the name of their corresponding spring in the spring model.

The mechanical response of the system to lateral actuation can be modeled using simple linear springs, as seen in Fig. 3.

The spring constant includes contributions from the tethers that run perpendicular to the direction of motion, the folded beam suspension attached to the actuation comb drive, the opposite folded beam suspension, and the bends in the tethers. The total lateral spring constant of the system is given below.

$$k_{total} = k_{folded} + k_1 \tag{3}$$

Where k_{folded} is the spring constant of the folded beam suspension, and k_1 is given by

$$k_1 = \left(\frac{1}{2k_{relief}} + \frac{1}{k_2 + 4k_{tether}} \right)^{-1} \tag{4}$$

and represents the spring constant of all flexures in parallel with the folded beam suspension attached to the actuation comb drive, as seen in Fig. 3. The spring constant of the strain relief is represented by k_{relief}, the spring constant of the off axis tether is represented by k_{tether} (this includes the bending of the off axis bimorphs), and the cumulative spring constant of the strain reliefs and the folded beam suspension on the opposite side of the plate from the actuation comb. It is given by

$$k_2 = \left(\frac{1}{2k_{relief}} + \frac{1}{k_{folded}} \right)^{-1} \tag{5}$$

The strain relief on the tether attached to the actuation comb drive stretches during actuation and this causes the plate to move less than the comb drive.

The ratio of the comb drive displacement to the lateral plate displacement is given by

$$\frac{x_{plate}}{x_{comb}} = \frac{k_1}{k_2 + 4k_{tether}} \tag{6}$$

The predicted ratio of x_{plate} to x_{comb} using optical measurements of dimensions and Comsol Multiphysics to predict the spring constants is 47%. The measured ratio is 64%. We attribute the difference largely to errors in component dimension measurements.

III. Performance

The measured displacement of the comb drive and the plate is seen in Fig. 4, and plate actuation is shown in air and vacuum. Fig. 4 also shows the vertical motion of the plate as it is moved laterally. The vertical motion is undesirable; however, as we will discuss below, there are multiple vertical actuation methods that can be used to correct it. Fits of the lateral data are also included. The motion follows a well known

$$x = cV^2 \tag{7}$$

relationship where x is lateral displacement, c is a constant and V is the potential difference across the comb drive. This relationship stems from (2) and the derivative of capacitance with respect to lateral displacement being constant. Comb drive actuation was measured via optical microscopy, plate actuation in vacuum was measured with a scanning electron microscope (SEM), lateral plate actuation in air was measured with optical microscopy, and vertical plate actuation in air was measured with an optical interferometer. All error bars are two

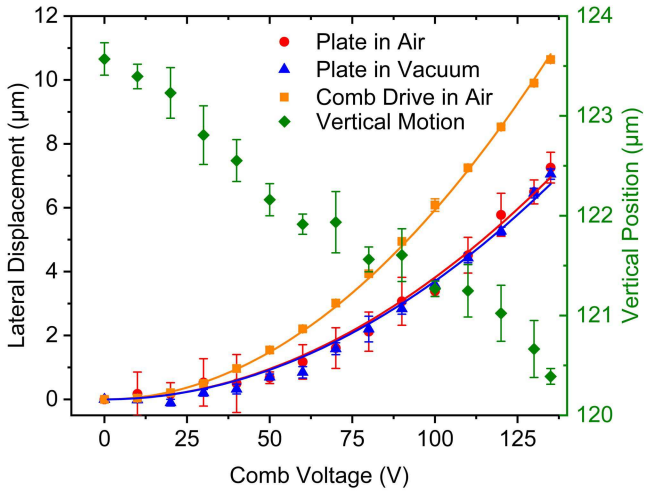

Fig. 4. Lateral actuation of the device obtained using the comb drives. Measured data and V^2 fits are shown for both air and vacuum actuation, for both the central plate and the comb drive itself. Because of an asymmetry in the electrostatic potential on the fingers of the comb drive and a torque on the bimorphs, there is a small vertical motion of the plate when the drives are actuated. Error bars represent twice the standard deviation above and below the average of three measurements.

standard deviations in both directions. The error bars for the plate motions are from three measurements (per data point) of different sections of a single scan. The error bars for comb drive motions come from three measurements as well, but each is measured from a different optical microscope image. For many data points, the error bars are smaller than the point. Supplemental Movie 1 (SM1) is a stop motion video of lateral actuation of a device. It is composed of a series of SEM images at different actuation potentials.

Vertical actuation is achieved by three different methods. 1) All comb drive actuation where all of the comb drives are actuated simultaneously causing a vertical drop in the plate. 2) Parallel plate actuation where a potential is placed on the top plate and the bottom plate and substrate are grounded causing the top plate to pull down towards the substrate. 3) Bimorph actuation where the bimorphs are heated causing them to lower towards the substrate.

In method one (all comb drive actuation), there are two effects that cause vertical displacement, as demonstrated in Fig. 5c. First, the lateral force applied at the base of the bimorphs by the comb drive and the restoring force applied at the top by the tethers generate a torque on the bimorphs that causes them to tilt and lowers the central plate. Second, there is a well-known levitation effect at the comb drive that occurs because of the grounding plane shielding fringe fields [24], [28], [29]. This effect results in a vertical force on the comb fingers and also causes the bimorphs to tilt, lowering the plate. The total range due to both of these effects is 9.2 μm. The actuation voltage vs. height data is plotted in Fig. 5a. Also plotted is the height data for a single comb that is also plotted in Fig. 4. Both datasets were measured using a white light interferometer, and the error bars are twice the standard deviation of three samples taken from different sections of the same scan. Supplemental Movie 2 (SM2) is a stop motion

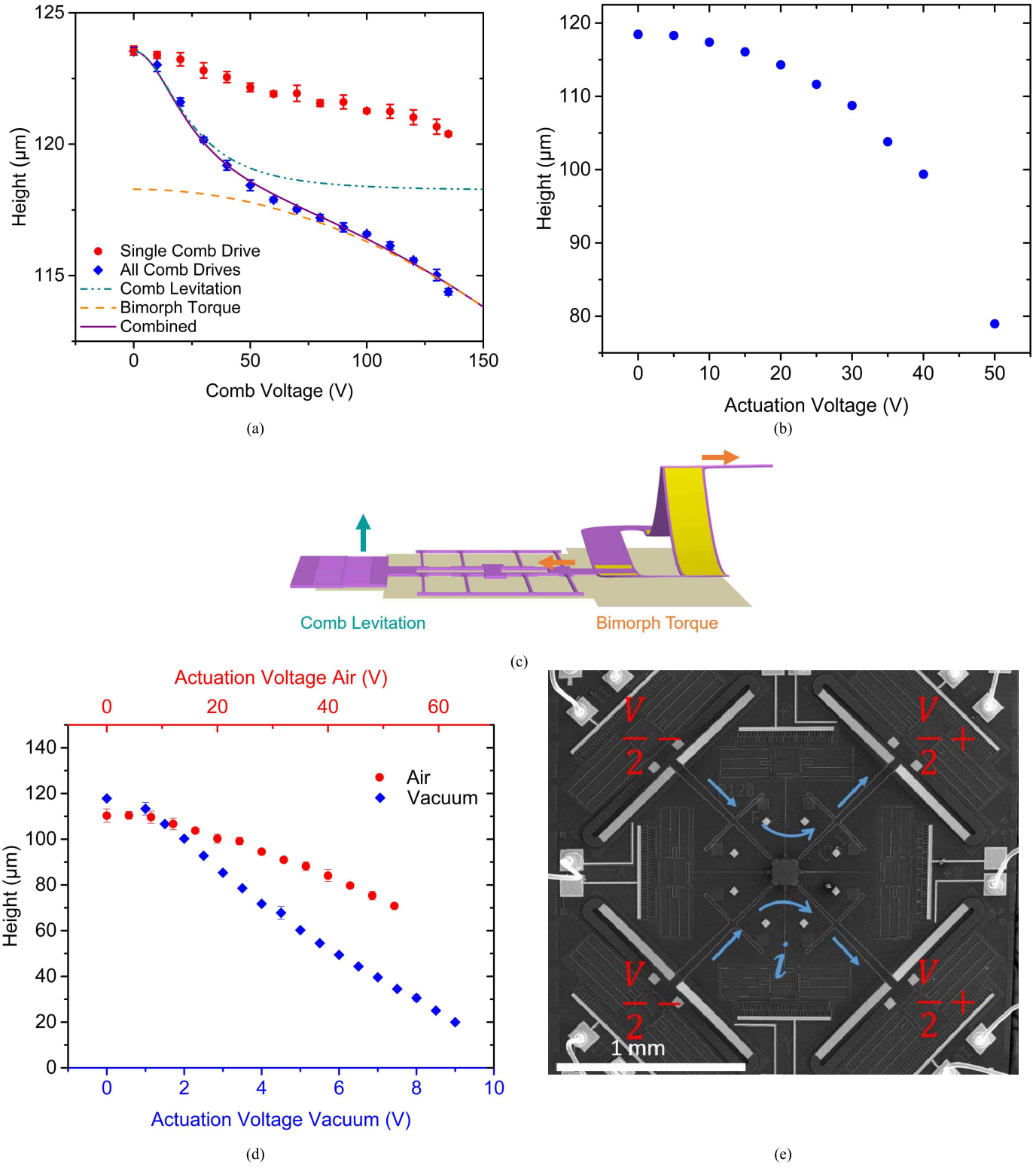

Fig. 5. Three methods of vertical actuation. (a) Plot of actuating all of the comb drives simultaneously also included is a fit based on two different mechanisms which are plotted individually and combined. (b) Plot of actuating by putting a potential difference between the plate and the substrate and electrostatically pulling the plate down. The plate pulled in at about one third the initial separation. (c) A diagram of one quadrant of the device showing the two mechanisms used to fit the data in (a). (d) Plot of actuating the thermal bimorphs by running a current through the tethers and folded beam suspensions in both air and vacuum. (e) SEM image of the device with the potentials and currents used in (d) labeled. The potential difference plotted in (d) is the total potential difference.

video of this actuation method, similar to SM1.

Also plotted in Fig 5a are a series of fits showing that the shape of the displacement curve is well predicted by the theoretical shapes that would be expected by the explanations

given. At low voltages, the torque is low and the comb drive levitation effect dominates the slope. This switches at 50 V. The levitation effect's curve was obtained using (2) and setting it equal to the restoring force of the spring for vertical and lateral displacements as seen in (8) and (9).

$$k_x x = \frac{1}{2}\frac{\partial C}{\partial x}V^2 \tag{8}$$

$$k_z z = \frac{1}{2}\frac{\partial C}{\partial z}V^2 \tag{9}$$

The derivatives of capacitance were obtained by modeling change in capacitance with displacement in Comsol Multiphysics. A simple second order polynomial function was used to fit this data and then obtain the derivatives. This simulation data and polynomial fit is in supplemental materials section S4. By solving the system of equations, vertical displacement (z) in terms of V was found. There is an additional scaling factor necessary to convert between vertical motion of the comb drive and vertical motion of the plate. A Comsol FEA simulation predicted the scaling factor to be 1.94. The scaling factor that fit the data was 3.58. We attribute the difference to errors in measurements of physical dimensions and FEA modeling.

The torque effect was modeled simply by multiplying the comb drive fit in Fig. 4 by a linear scaling factor. A Comsol model predicted that the scaling factor should be 0.330. The value that best fits the data is 0.335.

Method two uses parallel plate capacitive actuation by putting a potential on the plate and grounding the bottom plate and substrate. The height versus potential is measured with white light interferometry and plotted in figure 5b. The measured actuation range is 39.5 μm after which pull in occurs. This is approximately one third of the initial height, which is the pull in distance predicted for a parallel plate actuator balanced by a spring [15]. This method is complicated in applications where there is a second substrate above the plate is present, as in atomic calligraphy and SPM.

Method three utilizes the thermal bimorphs. As the bimorphs are heated, they bend towards the substrate due to the greater thermal expansion coefficient of the gold. In this design, the bimorphs are heated by running current through the tethers and the folded beam suspensions, as seen in Fig. 5e. By heating all of the bimorphs simultaneously the plate is moved down towards the substrate. Fig. 5d shows the height vs actuation voltage on the bimorphs in both air and vacuum.

Unlike electrostatic methods that yield almost indistinguishable results in air and vacuum, the vacuum actuation of the thermal bimorphs has a larger range and occurs at much lower voltages than the air actuation. This is because at atmospheric pressure additional heat is lost by conduction. The actuation range achieved in air is 39.5 μm at 52 V and in vacuum is 97.9 μm at 9 V. The vacuum actuation range is only limited by contacting structures underneath the plate. It is possible that the actual range is greater, but we were conservative with actuation voltages to avoid the plates getting stuck together in the electron microscope.

Air actuation on the other hand is limited due to electrostatic pull in of the base of the bimorph onto the substrate. The substrate is covered in a polysilicon layer that is connected electrically to the bimorphs via the folded beam suspension to help prevent electrostatic pull in. However, at larger actuation voltages the potential drop across the folded beam suspension creates a potential difference that causes the base of the bimorph to pull down and prevents lateral actuation. At the highest air actuation ranges reported here (before the base of the bimorphs pull in), some limiting of the lateral actuation begins to occur due to a combination of the electrostatic actuation between the base and the substrate and torque on the bimorphs generated in lateral actuation.

Air heights were measured with optical interferometry, and vacuum heights were measured in a SEM. In both cases, the error bars represent plus or minus twice the standard deviation of three different scans. For the vacuum data, only three data points have error bars plotted because the data points without error bars represent single measurements. Supplemental Movie 3 (SM3) is a stop motion video of this actuation method in vacuum.

Similar to the third method of vertical actuation, angular actuation is achieved using the thermal bimorphs. Running current between the returns of a pair of adjacent comb drives, as outlined in Fig. 6a, moves four of the eight thermal bimorphs towards the substrate causing the plate to tilt, as seen in Fig. 6b. Additionally, Supplemental Movie 4 (SM4) is a stop motion video of this actuation method. Because this method relies on the thermal bimorphs, different performance is found between air and vacuum environments. Both environments performances are plotted in Fig. 6c. Vacuum actuation was measured using an SEM and air actuation was measured by white light interferometry. The maximum actuation angles measured were 3.7° and 0.89° for vacuum and air respectively. Because the plate can be tilted in the opposite direction as well using the opposite four bimorphs, the total actuation range is twice the measured, or 7.4° and 1.8° for vacuum and air respectively.

The maximum operating frequency is different for the thermal and electrostatic actuation methods. Thermal methods are limited by the thermal time constant of the system. The bimorph can only move back up as quickly as it can cool. Electrostatic forces on the other hand are applied extremely rapidly, and the limit to the maximum operating frequency is the mechanical response of the system. Fig. 7 shows the normalized frequency response for a plate being actuated with the thermal bimorphs and being actuated with the all of the comb drives (vertical actuation methods 3 and 1 respectively). The response was measured by a laser vibrometer in air and both actuation methods moved the plate a similar amplitude. It can be seen in the figure that the response of the thermal bimorph begins falling off almost immediately, after 10 Hz, while the response of the all comb drive method does not begin to fall off until after the second major resonance peak at 3.2 kHz.

This result implies that the device can be positioned in <1 ms, potentially as fast as $\sim$100 μs using advanced drive techniques [30], [31]. Also, shown are the modes corresponding to each of the major peaks. These were obtained using Comsol Multiphysics.

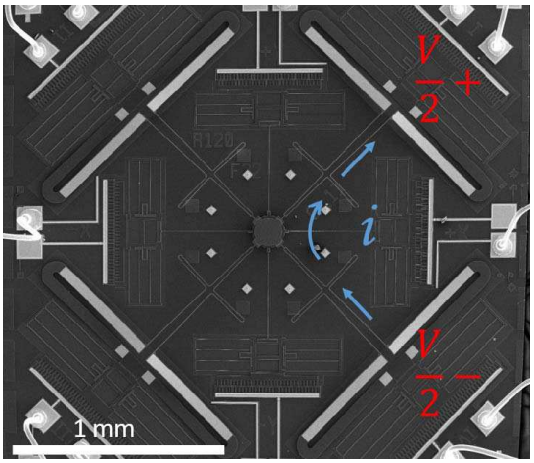

(a)

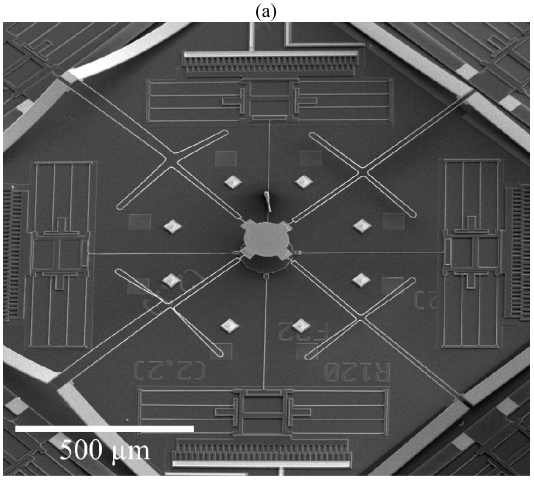

(b)

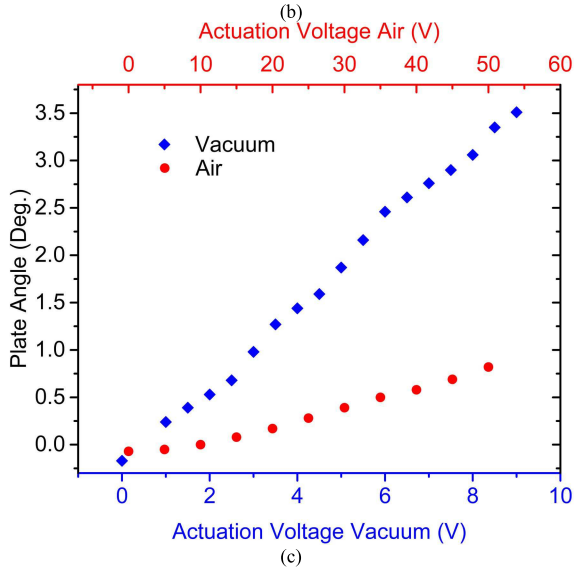

(c)

Fig. 6. Shown is the tip/tilt operation. (a) An SEM image of the device with the potentials and current paths used in tip/tilt operation labeled. (b) SEM image of the device at maximum tilt in vacuum. The bimorphs on the right are near the substrate. (c) Plot of the tilt angle versus voltage in vacuum and air. The actuation voltage is the total potential difference between V+ and V− in (a).

IV. Conclusion

We have presented a MEMS scanner with five degrees of freedom. It is capable of moving 14.1 μm ($\pm$7.1 μm) in both translational directions, 97.9 μm vertically, and 7.4° ($\pm$3.7°) in both tip and tilt, in vacuum. In air, it can move 14.1 μm ($\pm$7.1 μm) transitionally, 39.5 μm vertically, and 1.8° in tip and tilt. Vertical actuation can be achieved both with thermal methods that have long ranges but are slow and with electrostatic methods that have shorter ranges, but are capable of responding fully up to 3.2 kHz. Because this device is built by a low cost commercial foundry, it can inexpensively be modified and integrated into a variety of applications, and manufactured in both large and small quantities.

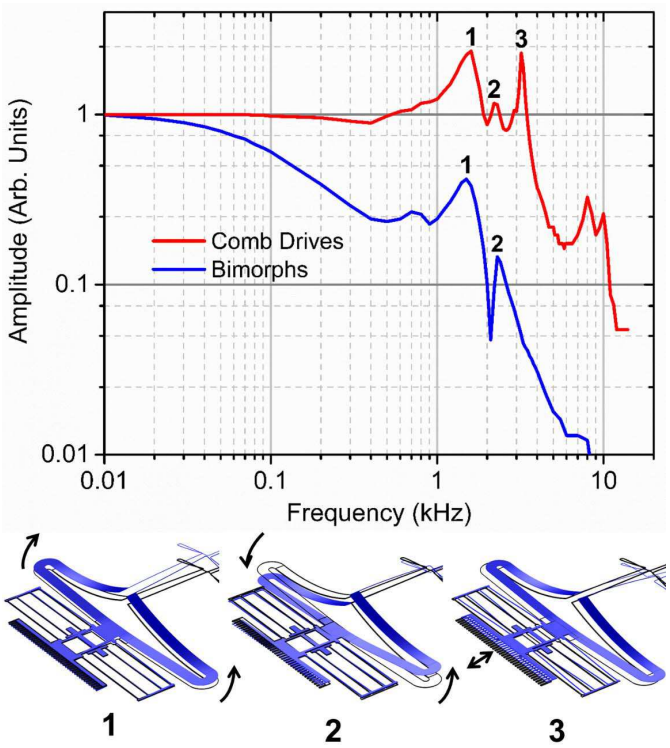

Fig. 7. Frequency response of the 5 DoF scanner. Comb drive actuation responds fully up to 3.2 kHz while actuation using thermal bimorphs begins to fall off above 10 Hz because the response speed is limited by the cooling rate. Below the graph are the various modes associated with the peaks (generated by a FEA in Comsol Multiphysics). Mode 1 is an up and down oscillation of the bimorphs where the bimorphs move in phase with each other. Mode 2 is also an up and down oscillation of the bimorphs, but the bimorphs move out of phase with each other. Mode 2 also possesses some small tilting of the structure. Mode 3 is a lateral in and out oscillation of the comb drive. The peak associated with this mode only appears in the response to the comb drive actuation because the bimorph actuation does not excite it.

Acknowledgment

We would like to thank the Boston University Photonics Center staff.

References

[1] V. A. Aksyuk, B. P. Barber, P. L. Gammel, and D. J. Bishop, "Construction of a fully functional NSOM using MUMPs technology," 1997, vol. 3226, pp. 188–194.

[2] V. A. Aksyuk, D. J. Bishop, and P. L. Gammel, "Micromechanical xyz stage for use with optical elements," US5963367A, 23-Sep-1997.

[3] Sunghoon Kwon and L. P. Lee, "Stacked two dimensional micro-lens scanner for micro confocal imaging array," in *Technical Digest. MEMS 2002 IEEE International Conference. Fifteenth IEEE International Conference on Micro Electro Mechanical Systems (Cat. No.02CH37266)*, 2002, pp. 483–486.

[4] H. Mansoor, Haishan Zeng, I. T. Tai, Jianhua Zhao, and Mu Chiao, "A Handheld Electromagnetically Actuated Fiber Optic Raster Scanner for Reflectance Confocal Imaging of Biological Tissues," *IEEE Trans. Biomed. Eng.*, vol. 60, no. 5, pp. 1431–1438, May 2013.

[5] D. Bishop, F. Pardo, C. Bolle, R. Giles, and V. Aksyuk, "Silicon Micro-Machines for Fun and Profit," *J. Low Temp. Phys.*, vol. 169, no. 5–6, pp. 386–399, Dec. 2012.

[6] Che-Heung Kim, Hee-Moon Jeong, Jong-Up Jeon, and Yong-Kweon Kim, "Silicon micro XY-stage with a large area shuttle and no-etching holes for SPM-based data storage," *J. Microelectromechanical Syst.*, vol. 12, no. 4, pp. 470–478, Aug. 2003.

[7] Y. Ando, "Development of three-dimensional electrostatic stages for scanning probe microscope," *Sensors Actuators A Phys.*, vol. 114, no. 2–3, pp. 285–291, Sep. 2004.

[8] N. Sarkar, R. R. Mansour, O. Patange, and K. Trainor, "CMOS-MEMS atomic force microscope," in *2011 16th International Solid-State Sensors, Actuators and Microsystems Conference*, 2011, pp. 2610–2613.

[9] H. Toshiyoshi, Guo-Dung John Su, J. LaCosse, and M. C. Wu, "A surface micromachined optical scanner array using photoresist lenses fabricated by a thermal reflow process," *J. Light. Technol.*, vol. 21, no. 7, pp. 1700–1708, Jul. 2003.

[10] J. B. Chou, N. Quack, and M. C. Wu, "Integrated VCSEL-Microlens Scanner With Large Scan Range," *J. Microelectromechanical Syst.*, vol. 23, no. 6, pp. 1471–1476, Dec. 2014.

[11] M. Imboden *et al.*, "Atomic Calligraphy: The Direct Writing of Nanoscale Structures Using a Microelectromechanical System," *Nano Lett.*, vol. 13, no. 7, pp. 3379–3384, Jul. 2013.

[12] M. Imboden *et al.*, "Building a Fab on a Chip," *Nanoscale*, vol. 6, no. 10, pp. 5049–5062, Apr. 2014.

[13] K. Kim, X. Liu, Y. Zhang, and Y. Sun, "Nanonewton force-controlled manipulation of biological cells using a monolithic MEMS microgripper with two-axis force feedback," *J. Micromechanics Microengineering*, vol. 18, no. 5, p. 055013, May 2008.

[14] P. Pan, W. Wang, C. Ru, Y. Sun, and X. Liu, "MEMS-based platforms for mechanical manipulation and characterization of cells," *J. Micromechanics Microengineering*, vol. 27, no. 12, p. 123003, Dec. 2017.

[15] C. Liu, *Foundations of MEMS*, 2nd ed. Prentice Hall, 2012.

[16] M. Maroufi, A. G. Fowler, and S. O. R. Moheimani, "MEMS for Nanopositioning: Design and Applications," *J. Microelectromechanical Syst.*, vol. 26, no. 3, pp. 469–500, Jun. 2017.

[17] X. Liu, K. Kim, and Y. Sun, "A MEMS stage for 3-axis nanopositioning," *J. Micromechanics Microengineering*, vol. 17, no. 9, pp. 1796–1802, Sep. 2007.

[18] G. Xue, M. Toda, and T. Ono, "Comb-Drive XYZ-microstage With Large Displacements Based on Chip-Level Microassembly," *J. Microelectromechanical Syst.*, vol. 25, no. 6, pp. 989–998, Dec. 2016.

[19] Jingyan Dong and P. M. Ferreira, "Electrostatically Actuated Cantilever With SOI-MEMS Parallel Kinematic XY Stage," *J. Microelectromechanical Syst.*, vol. 18, no. 3, pp. 641–651, Jun. 2009.

[20] B. Koo, J. E. Correa, and P. M. Ferreira, "Parallel-kinematics XYZ MEMS part 2: Fabrication and experimental characterization," *Precis. Eng.*, vol. 46, pp. 147–157, Oct. 2016.

[21] S.-C. Chen and M. L. Culpepper, "Design of a six-axis micro-scale nanopositioner—μHexFlex," *Precis. Eng.*, vol. 30, no. 3, pp. 314–324, Jul. 2006.

[22] J. Correa, B. Koo, and P. Ferreira, "Parallel-kinematics XYZ MEMS part 1: Kinematics and design for fabrication," *Precis. Eng.*, vol. 46, pp. 135–146, 2016.

[23] M. Imboden and D. Bishop, "Top-down nanomanufacturing," *Physics Today*, vol. 67, no. 12, American Institute of Physics, pp. 45–50, 30-Dec-2014.

[24] M. Imboden, J. Morrison, E. Lowell, Han Han, and D. J. Bishop, "Controlling Levitation and Enhancing Displacement in Electrostatic Comb Drives of MEMS Actuators," *J. Microelectromechanical Syst.*, vol. 23, no. 5, pp. 1063–1072, Oct. 2014.

[25] A. Cowen, B. Hardy, R. Mahadevan, and S. Wilcenski, "PolyMUMPs Design Handbook a MUMPs®process."

[26] A. Syed, L. Mu, M. Shavezipur, and P. Nieva, "Eliminating the galvanic effect for microdevices fabricated with PolyMUMPs®," in *2008 1st Microsystems and Nanoelectronics Research Conference*, 2008, pp. 197–200.

[27] W.-H. Chu, M. Mehregany, and R. L. Mullen, "Analysis of tip deflection and force of a bimetallic cantilever microactuator," *J. Micromechanics Microengineering*, vol. 3, no. 1, pp. 4–7, Mar. 1993.

[28] P. G. del Corro, M. Imboden, D. J. Bishop, and H. Pastoriza, "Comb Drive Designs With Minimized Levitation," *J. Microelectromechanical Syst.*, vol. 25, no. 6, pp. 1025–1032, Dec. 2016.

[29] W. C. Tang, M. G. Lim, and R. T. Howe, "Electrostatic Comb Drive Levitation And Control Method," *J. Microelectromechanical Syst.*, vol. 1, no. 4, pp. 170–178, Dec. 1992.

[30] M. Imboden *et al.*, "High-Speed Control of Electromechanical Transduction: Advanced Drive Techniques for Optimized Step-and-Settle Response of MEMS Micromirrors," *IEEE Control Syst.*, vol. 36, no. 5, pp. 48–76, Oct. 2016.

[31] C. Pollock *et al.*, "Engineered PWM Drives for Achieving Rapid Step and Settle Times for MEMS Actuation," *J. Microelectromechanical Syst.*, vol. 27, no. 3, pp. 513–520, Jun. 2018.